Pushbroom satellite image super-resolution using generative adversarial networks

Chao Xu
The Chinese University of Hong Kong
Shatin, New Territories, Hong Kong SAR
1155160618@link.cuhk.edu.hk

Abstract

In order to improve the resolution or visual effect of imageries from pushbroom sensors, this report proposes to use super-resolution generative adversarial networks (SRGAN) [6]. Some improvements are achieved: firstly, the VGG-19 [9] network is modified to extract the features of input images, and thus reduce the training time; secondly, the loss function is updated as new evaluation metric for the generated images; finally, three models with different hyperparameters are trained and compared to find the optimal results. In this report, the pushbroom image super-resolution is achieved with a scale factor of 4, and the result shows a better visual perception compared with that recovered by bicubic interpolation. We call the network model in this report as pbiSRGAN, which is Push-Broom Images SRGAN.

1. Introduction

Pushbroom imaging has been one of the most common satellite scanning methods over the past decades, which features in low manufacturing cost and relatively high maneuvering [11]. However, its spatial resolution is usually degraded due to strong atmospheric turbulences, fierce temperature fluctuation or the Earth rotation, et al. As the development of CMOS and CCD technology, the size of single detector pixel is getting smaller and the density of detector array is increasing, which help improve the satellite image resolution but also greatly level up the hardware manufacturing cost. Therefore, software methods such as imaging super-resolution algorithms have been proposed recently.

Conventional super-resolution methods include nonuniform interpolation, maximum a posteriori, projection on convex sets, and iterative back projection [7]. These methods have their own constraints, such as multiple solutions, instability or image blurring. Since the beginning of this decade, deep learning has been keeping advancing itself into various areas, including object detection, image classification, speech recognition and so on. Imaging super-resolution has been a hot topic in the deep learning community since it is first introduced in 2015 as SRCNN [1]. In 2017, a perceptual loss is additional proposed in SRGAN [6] as a complement to the conventional pixel-based loss metrics, and it is another landmark in the area of deep learning image super-resolution. Essentially, the SRGAN method is also a variant of GAN proposed in 2014 [2].

In this report, we will first talk about the basic principle of SRGAN, which is different from those methods generating images pixelwisely, but creates more visually perceptual images with high resolution. Secondly, a neural network architecture for pushbroom images is described, including how it is fit for gray-scale remote sensing imageries, how to reduce training time and improve training efficiency. Finally, three experimental groups will be set up with different hyper-parameters to find the optimal results for the pbiSRGAN.

2. Key concept of SRGAN

As for SRGAN, the low-resolution images are fed into the generation network and ”high-resolution images” are generated as the input of the discriminant network. The discriminator needs to determine whether the input images are generated ”high-resolution image” or the original ground truth value. The super resolution process is completed when the equal probabilities are obtained of ”high-resolution images” being judged as true or false. At this time, the generative network can be used to generate the ”high-resolution images” closest to the ground truth value. Here, it is also necessary to mention the way of ”summarizing experience” for both networks, namely, loss function. The loss function used in SRGAN is critical to the final network, which is different from the traditional per-pixelwise MSE loss. It evaluates the generated image from the perspective of human visual perception [6]. The advantage of pixelwise MSE loss is that it achieves a very high PSNR, but the reconstructed images are lack of high-frequency information, resulting in over-smooth image texture and poor visual effect. Specifically, the perceptual loss function L^{SR} is composed of content loss L^{SR}_{Con} and weighted generative loss L^{SR}_{Gen}:

$$L^{SR} = \underbrace{\underbrace{L^{SR}_{\text{Con}}}_{\text{content loss}} + \underbrace{10^{-3} L^{SR}_{\text{Gen}}}_{\text{generative loss}}}_{\text{perceptual loss}} \tag{1}$$

Content loss uses VGG-19 [9] as the feature extractor of the input image. The pre-trained network has strong feature extraction capability. Content loss is defined as the Euclidean distance between the reconstructed image $G(I^{LR})$ and the reference image I^{HR} feature map:

$$L^{SR}_{Con} = \sum_{x=1}^{W_{i,j}} \sum_{y=1}^{H_{i,j}} \left(\phi_{i,j}\left(I^{HR}\right)_{x,y}, \phi_{i,j}\left(G\left(I^{LR}\right)\right)_{x,y}\right)^2 \tag{2}$$

where $W_{I,j}$ and $H_{I,j}$ respectively represent the dimensions of each feature map in VGG-19 network; $\phi_{i,j}$ refers to the feature map [6] obtained by the convolution layer j in front of the max pooling layer i in VGG-19 network.

The other part of the perceptual loss is generative loss, which makes the generated results more consistent with the real images of human visual perception.

$$L^{SR}_{Gen} = \sum_{n=1}^{N} -\log D\left(G\left(I^{LR}\right)\right) \tag{3}$$

where $D(G(I^{LR}))$ is defined as the probability that the discriminator D determines the reconstructed images as real high resolution images, and N is the number of generated samples.

3. From SRGAN to pbiSRGAN

Compared with natural images, there is a serious problem applying SRGAN to remote sensing pushbroom images, that is, the lack of real training sets containing high-low resolution image pairs. Specifically, if the real image obtained by the satellite is regarded as a low-resolution image, and then it is impossible to obtain the corresponding ground truth as a high-resolution image. It is obvious that the satellite cannot avoid atmospheric turbulence, temperature fluctuation and other factors in the real-scene shooting, therefore, it is impossible to obtain a higher resolution image. The only way to get high-low resolution image pair is to take the real satellite image as a high-resolution image (i.e., ground truth) and then simulate a low-resolution version of it. In addition, SRGAN is originally proposed to solve the super-resolution problem of naturally colorful images, and can not be directly used for remote sensing data. Remote sensing images can be divided into panchromatic, multispectral, hyperspectral and even hyperspectral data, whose image channels range from one to hundreds. The remote sensing imageries own the characteristics of large scanning scale and great data volume, and the coverage of a single shot can reach dozens or even hundreds of square kilometers. Therefore, we proposed pbiSRGAN to achieve the purpose of super-resolution for pushbroom scanning remote sensing images.

4. Training and reconstructing of pbiSRGAN

The section aim to training and reconstructing process of remote sensing image super-resolution.

4.1. pbiSRGAN training flow

The training flowchart is shown in Fig. 1 for model of pbiSRGAN.

In the first step, a panchromatic remote sensing image used and preprocessed to make it as the initial ground truth of network input. The steps of preprocessing include histogram equalization and random cutting. The former aims to improve the contrast of the image and is beneficial to the extraction of the feature map. The latter is to generate sufficient data sets, including training sets, validation sets, and testing sets.

Second, after the training set enters the network, bicubic interpolation with a certain scale factor is conducted to generate the corresponding low-resolution images (namely, the high-resolution images are downsampled), and thus obtaining the HR and LR image pairs in the training process.

The third step is to train the generative network G. The low-resolution image LR is passed through G to get "generated high-resolution image" $G(I^{LR})$. Since the network G is weak at first, the quality of $G(I^{LR})$ may not be as good as LR. Here, we need to evaluate the loss of the generated image. L^{SR}_{G}, which is the loss of the network G, is mainly divided into two parts, namely the content loss L^{SR}_{Con} and generative loss L^{SR}_{Gen}.

L_{Con}^{SR} is evaluated by Eq.(4):

$$L_{Con}^{SR} = \sum_{x=1}^{W_{i,j}} \sum_{y=1}^{H_{i,j}} \left\| \phi_{i,j}\left(I^{HR}\right)_{x,y}, \phi_{i,j}\left(G\left(I^{LR}\right)\right)_{x,y} \right\|_1 \quad (4)$$

That is, the feature maps of $G(I^{LR})$ and HR are extracted through the modified VGG-19 network, and the L_1 distance between them is calculated. The L_2 norm is mainly related with the Gaussian distribution error, while the L_1 norm is related to the Laplace error. When the image contains non-Gaussian errors, the confidence of L_1 norm is higher than that of L_2 norm [10]. Only when the error of the model is Gaussian white noise distribution, the solution of L_2 model is optimal, which is difficult to achieve in real world. L_{Gen}^{SR} is also redesigned as shown in Eq.(5):

$$L_{Gen}^{SR} = \sum_{n=1}^{N} 1 - \log D\left(G\left(I^{LR}\right)\right) \quad (5)$$

Therefore, we update the perceptual loss function L_G^{SR} of generative network G.

$$L_G^{SR}{=}L_{Con}^{SR}{+}10^{-3}L_{Gen}^{SR} \quad (6)$$

Finally, we need to train the discriminator D. The power of network D can be strengthened by iteration of the loss function L_D^{SR}, which consists of two parts, L_{real}^{SR} to discriminate I^{HR} as true and L_{fake}^{SR} to discriminate $G(I^{LR})$ as false.

$$L_{real}^{SR} = \sum_{n=1}^{N} 1 - \log D\left(I^{HR}\right) \quad (7)$$

$$L_{fake}^{SR} = \sum_{n=1}^{N} - \log D\left(G\left(I^{LR}\right)\right) \quad (8)$$

$$L_D^{SR} = \frac{1}{2}\left(L_{real}^{SR} + L_{fake}^{SR}\right) \quad (9)$$

4.2. pbiSRGAN reconstructing flow

While validating the generative networks using validation set, super-resolution reconstruction can also be accomplished, as shown in Fig. 2.

5. Network architecture of pbiSRGAN

The network is mainly divided into three parts: feature extraction network F, generative network G and discriminant network D.

5.1. Feature extraction network

The basic prototype of the feature extraction network comes from the VGG-19 network, which is a 19-layer pre-training network with very strong feature extraction ability, but it cannot be directly applied to the network model in this project. VGG-19 is used for feature extraction of colorful images. In this section, the previous 18 layers of VGG-19 are extracted, and the first layer of VGG-19 is modified into a structure suitable for single-channel gray remote sensing images. In this way, the feature extraction network F can obtain the corresponding features from the ground truth value and generated images, and then carry out loss calculation. The structure of network F is shown in Fig. 3.

5.2. Generative network

Generative network G is the core of the whole pbiSRGAN network, which will generate high-resolution images. The network structure we designed is shown in the Fig. 4, the core of which is the residual block. The role of residual blocks will be discussed later.

Specifically, a convolution layer with kernel size of 9×9 is used first, and the input is a single-channel low-resolution image and the output is a 64-channel feature map. A Parametric Rectified Linear Unit (PRELU) is then used as the activation function, with the parameter of . As shown in Fig. 5, PRELU is actually a variant of Leaky Rectified Linear Unit (Lrelu). For LReLU, if $x < 0, y = 0.01x$;For PReLU, if $x < 0$, then $y = ax$. Compared with ReLU, the advantages of using PReLU are to prevent zero activation of the network and speed up the training process.

Next, we use 16 residuals blocks, all of which have the same structure. Using residuals blocks helps solve the optimization problem when the forward network is too deep [3]. The structure of each residual block is shown in Fig. 6. Its first layer is a convolution layer, with input and output channels of 64, and the size of the convolution kernel is 3 *times*3. What follows up is a batch normalization (BN) layer that speeds up training by reducing covariance shifts within the dataset, allowing us to use larger learning rates during training without decreasing output quality[4]. After activation by PRELU, there is another pair of convolution layer and batch normalization layer with the same parameters as above, and the final output is 64-channel feature map.

As shown in the Fig. 4, after passing the output of the PReLU1 layer and the 16 residual blocks to the BN33 layer, we used two trained sub-pixel convolution layers to increase the resolution of the input image [8]. The core of the sub-pixel convolution layer is the PixelShuffle layer, which can convert the 4-dimensional data in the training process from $(*, C \times r \times r, H, W)$ to $(*, C, H \times r, W \times r)$, where $*$ represents the batch size of the data set. C, H and W are the dimension of the images, and r is the scale factor. Finally, the generated high-resolution image is obtained through the Conv37 layer.

5.3. Discriminant network

The main function of discriminant network D is to battle with generative network G, so as to improve the power of G. The discriminant network designed in this project is shown in the Fig. 7, with a total of 24 layers.The initial input channel and the final output channel are both designed as 1. In addition, the convolution layer of 64, 128, 256 and 512 channels is designed to gradually improve the feature extraction ability. The detailed parameters can be seen in Table 1.

6. pbiSRGAN experimental simulation

The section verifies the proposed model using single channel pushbroom remote sensing images.

6.1. Experimental environment

The parameters of hardware is shown in Table 2.

6.2. Experimental data

For the source dataset, the source image is obtained by a satellite pushbroom scanning method with multiple stitches. Its original size is 1 x 1197 x 50500. We will randomly crop the source image and generate the training, validation and testing dataset. In this case, we will generate 96000 training images, 3000 validation images, and 1000 testing images, respectively, with the shape of 1 x 128 x 128 as ground truth. The degraded images will be generated from the downsampling and upsampling of the ground truth. Here the scaling factor is 4.

6.3. Experimental scheme

In the verification simulation, three groups will be set up as shown in Table 3. Specifically, the total number of training epochs is set as 100. The batch size of the training set is 128, so the number of iterations in each epoch is 750. The batch size of the validation set is 1, and the number of iterations in each epoch is 3000. During the training process, the optimizer is ADAM [5], $\beta_1 = 0.5$, $\beta_2 = 0.999$, and the learning rates of generative and discriminant network are set as 0.0002. For Group 2, the learning rate is decreased by 90% at the 50th epoch. Our training method for the whole network is as follows: in each epoch, we trained the generator once and then trained the discriminator once, and carried out a total of 750 iterations; After that, the parameters of the generative network were fixed, and reconstructed images were generated and evaluated using this generator. A total of 3000 iterations should be carried out, and then we go to the next epoch. For Group 3, we test the generative network for 5 times and the discriminant network for 1 time. In the training, the parameters of feature extraction network F, generative network G and discriminant network D are 2324416, 1529748 and 4692545, respectively.

6.4. Experimental results

In view of the three experimental schemes proposed in this project, loss metric and reconstructed image evaluation will be adopted respectively, and the appropriate scheme will be finally selected.

6.4.1 Loss metric evaluation

The loss evaluation is mainly divided into two parts. One is the average loss of each batch in the process of model training, which is divided into five kinds of losses.The second is the average loss of each epoch during the training and validation process, and there are also 5 kinds of losses. Specific loss classification is shown in Table 4. For batch losses, the abscissa is the number of iterations with a maximum of 750, whose product with the training batch size is the training set size. After an epoch of training is completed, the model will record the batch loss of the previous epochs and average it with the batch loss of the current iteration number, so that the batch loss of the current iteration number can be obtained. The ordinate is the value of each batch loss.

The loss of the generative network is shown in Fig. 8 - Fig. 10 .For batch content loss, the loss value of Group 1 decreases faster. In the 200th iteration, the loss value of Group 1 is less than 0.025, while both Group 2 and 3 fail to reach this value. After 750 iterations, the final loss value of Group 1 is also smaller, reaching 0.024; the final loss values of Group 2 and 3 are 0.04 and 0.025, respectively. However, from the perspective of loss stability, the effect of Group 2 is better than that of Group 1 and 3.

For batch generation loss, the optimal value of Group 1 and 2 can be reached in the first 20 iterations, while the optimal value of Group 3 is reached in 100th iteration. For Group 1, the problem is that the losses fluctuate significantly in the 25th and 60th cycle. Similar problems exist in all the three groups.

According to the Eq. (6), content loss is the main component of the perceptual loss function. In addition, it can also be seen from the Fig. 9 that generative loss mainly plays a regulating role in the early training period. Therefore, the trend of the curve in Fig. 10 is basically the same as that in Fig. 8.

L_{real}^{SR} refers to the probability for determining a high resolution image to be true, and L_{fake}^{SR} refers to the probability for determining the generated image to be false. Eq. (7) and (8) indicate that the smaller the two values are,the stronger performance of the discriminant network appears. The discriminant loss L_{D}^{SR} is the average of the sum of L_{real}^{SR} and L_{fake}^{SR}. The same conclusion as above can also be obtained from the Fig. 11 - Fig. 13 : Group 1 converges faster but has stronger volatility compared with the other two groups.

Now, let's look at each loss process from the perspective of epoch. As shown in Fig. 14, with respect to the content loss, after training and validation of 100 epochs, the loss of Group 1 can be reduced to 0.02, while with the same epoch, the values of Group 2 and Group 3 can only reach 0.041 and 0.032. Group 1 is optimal only in terms of the minimum loss without considering the stability.

As shown in Fig. 15, for epoch generative loss, its curve trend is similar to that of batch generative loss. Group 1 can reach the optimal value at the second epoch, while for Group 2 and 3, this optimal value first appears at the 5th and 20th epoch, respectively. However, both Group 1 and 3 have a loss slump in the subsequent epoch, which is not suitable to create a stable model.

As shown in Fig. 16, after the training of 100 epochs, the final epoch perceptual loss of Group 1 can reach 0.022, still better than that of Group 2 (0.042) and Group 3 (0.034). This result is basically consistent with the batch perceptual loss.

It can be observed that in the process of discrimination, true and fake determination almost reach the optimal value at the same time, which can be seen from Fig. 17(a), Fig. 18(a) and Fig. 19(a) of Group 1 that the first optimal value appears near the 15th epoch. For Group 2 and 3, this value appears around the 18th and 40th epoch, respectively.

After the above comparison, we can conclude that Group 2 is the best and Group 1 is the worst from the perspective of model stability. If there is not enough training time to make the final model optimal, and the predictability of the model is pursued, Group 2 should be our choice. When we choose a trained model for reconstruction, even if the effect is not optimal, we can still predict the optimization direction of the next model, and this judgment is difficult to apply to Group 1. Of course, if there are sufficient training time and machine resources, all the final indicators of Group 1 are the best, and the reconstruction result should be the best, which can be the optimal choice.

6.4.2 Reconstructed image evaluation

Next, each group will be compared according to the quality of reconstructed images, and the reconstruction ability of the three models on the validation and testing set will be observed after the training of 100 epochs.

For the validation set, three scenes of oil tank, steel and roof are selected for super-resolution reconstruction, representing arc, linear and contrast features respectively, to verify the adaptability of the model under different environments. The reconstruction results are as follows: 20 for Group 1; 21 for Group 2; and 22 for Group 3.

For the representation and reconstruction capabilities of different features, Fig. 20 from Group 1 is taken as an example. The model shows the best performance for light and shadow features, especially the edge features with obvious contrast, which can be seen in the reconstructed roof image. Secondly, as for the linear features, the model can basically remove the blurring in the reconstructed steel image, but there is still some ringing effect. In addition, the performance of the super-resolution network is poor on the circular features, and the edges of the reconstructed oil tank image are blurred seriously, while the adjacent linear wall is not blurred so strongly.

Next, the reconstruction ability of the three models can be compared. It should be noted that during validation it is difficult to find identical subgraphs in different batches. Therefore, Fig. 20, Fig. 21 and Fig. 22 show three identical features, but the image content between them is not exactly the same. However, it has little impact on our evaluation. After the training of 100 epochs, the reconstruction result of Group 1 is the best, followed by Group 2 and Group 3. This conclusion can also be reached through two objective image quality evaluation indicators, the Peak Signal Noise Ratio (PSNR) and Structural Similarity (SSIM), as shwon in Fig. 23 and Fig. 24, respectively. At the 100th epoch, the average PSNR and SSIM of reconstruction results of Group 1 are 18.6049 and 0.6022. For Group 2, these two values are 16.7754 and 0.5161, and 15.3766 and 0.4569 for Group 3.

Finally, the average PSNR and SSIM of 1000 images in the testing set by three models are shown in Table 5. It can be seen that no matter in the validation or testing set, the performance of Group 1 is the best, followed by Group 2, and finally Group 3. Considering that there are sufficient computing resources and computation time at present, we decide to adopt Group 1 as the final scheme of the super-resolution neural network model in this project. On the testing set, some results obtained by reconstruction of Group 1 are shown in Fig. 25.

7. Conclusion

In this report, a super-resolution network model pbiSRGAN for remote sensing pushbroom image is proposed. When determining network parameters, three different schemes are designed, whose variables are learning rate, training ratio of generative and discriminant network, and other hyper-parameters are consistent. To judge the pros and cons of the three groups, the best scheme is obtained by comparing the result of loss function and reconstruction image effect. For the finally determined network model, the PSNR and SSIM obtained on the validation set are 18.6049 and 0.6022 respectively, while 19.6652 and 0.6045 on the testing set. In this report, the preset theoretical value of the super-resolution factor is 4. However, limited by the development of the existing aerospace hardware, the expected effect may still not be fully achieved in real scene use. However, on the whole, the reconstructed image has a good visual effect, greatly restoring the features of the original image.

Project webpage

You can find the code for this project here: https://github.com/chaoxu0512/Pushbroom-satellite-image-SRGAN.

No.	Layer	Input channel	Output channel
1	Conv2d	1	64
2	LeakyReLU	-	-
3	Conv2d	64	64
4	BatchNorm2d	64	64
5	LeakyReLU	-	-
6	Conv2d	64	128
7	BatchNorm2d	128	128
8	LeakyReLU	-	-
9	Conv2d	128	128
10	BatchNorm2d	128	128
11	LeakyReLU	-	-
12	Conv2d	128	256
13	BatchNorm2d	256	256
14	LeakyReLU	-	-
15	Conv2d	256	256
16	BatchNorm2d	256	256
17	LeakyReLU	-	-
18	Conv2d	256	512
19	BatchNorm2d	512	512
20	LeakyReLU	-	-
21	Conv2d	512	512
22	BatchNorm2d	512	512
23	LeakyReLU	-	-
24	Conv2d	512	1

Table 1: Parameters of discriminant network.

References

[1] C. Dong, C. C. Loy, K. He, and X. Tang. Image super-resolution using deep convolutional networks. IEEE transactions on pattern analysis and machine intelligence, 38(2):295–307, 2015.

[2] I. Goodfellow, J. Pouget-Abadie, M. Mirza, B. Xu, D. Warde-Farley, S. Ozair, A. Courville, and Y. Bengio. Generative adversarial nets. In Advances in neural information processing systems, pages 2672–2680, 2014.

[3] S. Gross and M. Wilber. Training and investigating residual nets. Facebook AI Research, 2016.

[4] S. Ioffe and C. Szegedy. Batch normalization: Accelerating deep network training by reducing internal covariate shift. arXiv preprint arXiv:1502.03167, 2015.

[5] D. P. Kingma and J. Ba. Adam: A method for stochastic optimization. arXiv preprint arXiv:1412.6980, 2014.

[6] C. Ledig, L. Theis, F. Huszár, J. Caballero, A. Cunningham, A. Acosta, A. Aitken, A. Tejani, J. Totz, Z. Wang, et al. Photo-realistic single image super-resolution using a generative adversarial network. In Proceedings of the IEEE conference on computer vision and pattern recognition, pages 4681–4690, 2017.

[7] S. C. Park, M. K. Park, and M. G. Kang. Super-resolution image reconstruction: a technical overview. IEEE signal processing magazine, 20(3):21–36, 2003.

[8] W. Shi, J. Caballero, F. Huszár, J. Totz, A. P. Aitken, R. Bishop, D. Rueckert, and Z. Wang. Real-time single image and video super-resolution using an efficient sub-pixel convolutional neural network. In IEEE conference on computer vision and pattern recognition, pages 1874–1883, 2016.

[9] K. Simonyan and A. Zisserman. Very deep convolutional networks for large-scale image recognition. arXiv preprint arXiv:1409.1556, 2014.

[10] H. Song, L. Zhang, P. Wang, K. Zhang, and X. Li. An adaptive l 1–l 2 hybrid error model to super-resolution. In 2010 IEEE International Conference on Image Processing, pages 2821–2824. IEEE, 2010.

[11] C. Xu, X. Yang, T. Xu, L. Zhu, L. Chang, G. Jin, and X. Qi. Study of space optical dynamic push-broom imaging along the trace of targets. Optik, 202:163640, 2020.

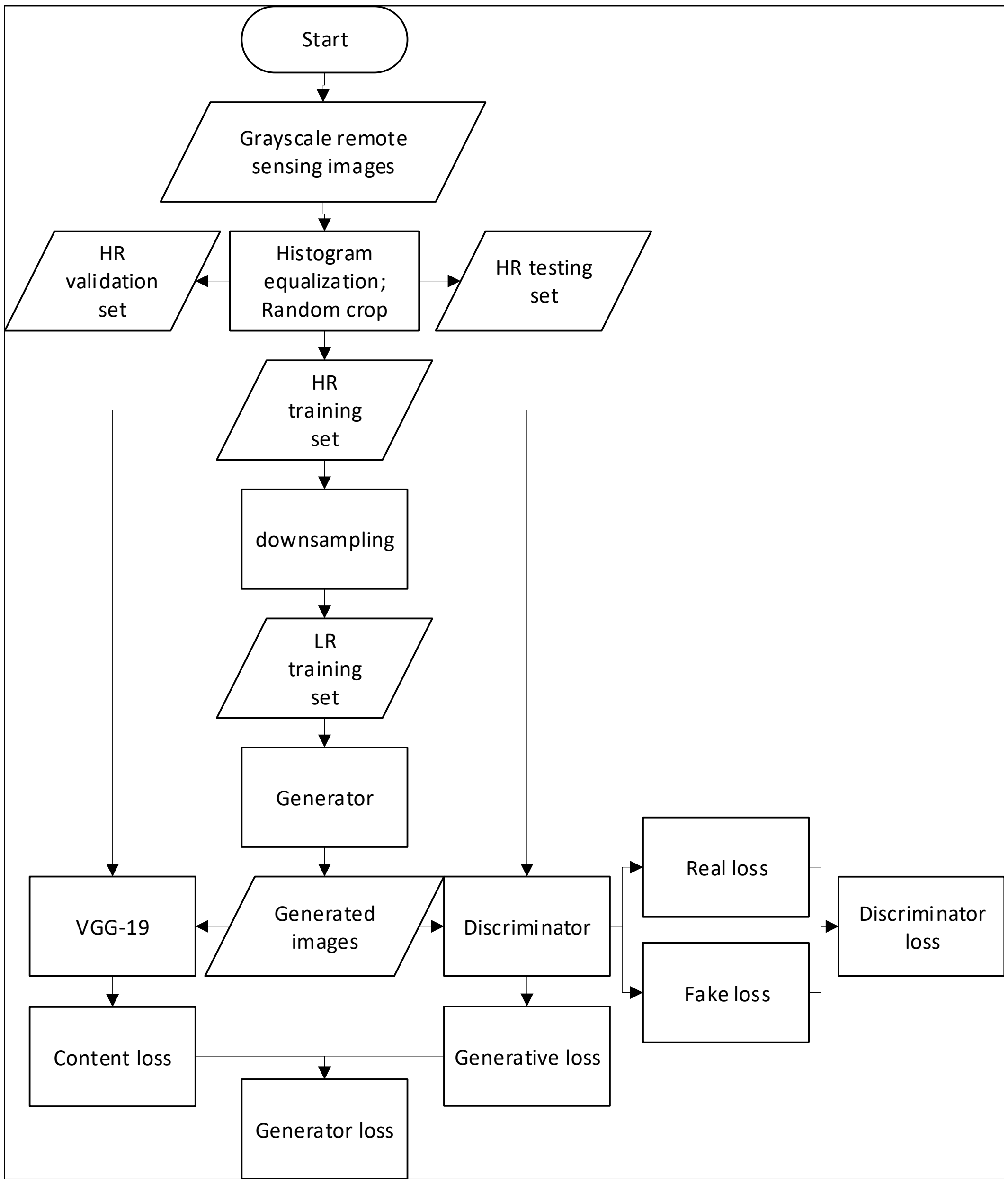

Figure 1: Training flow chart of pbiSRGAN.

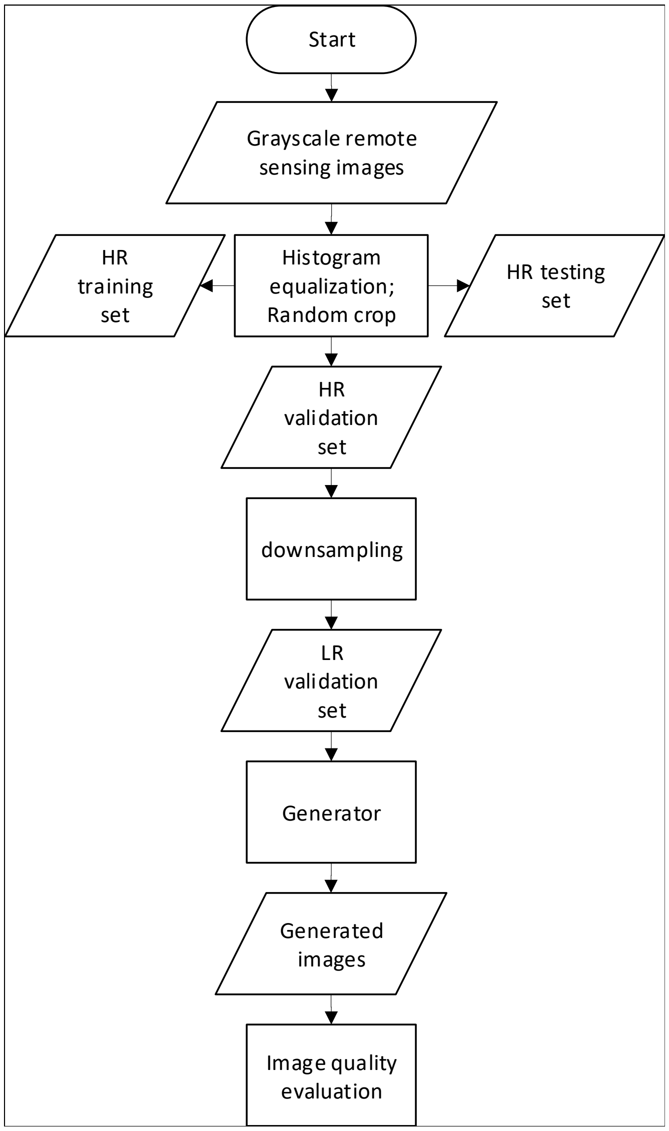

Figure 2: Reconstructing flow chart of pbiSRGAN.

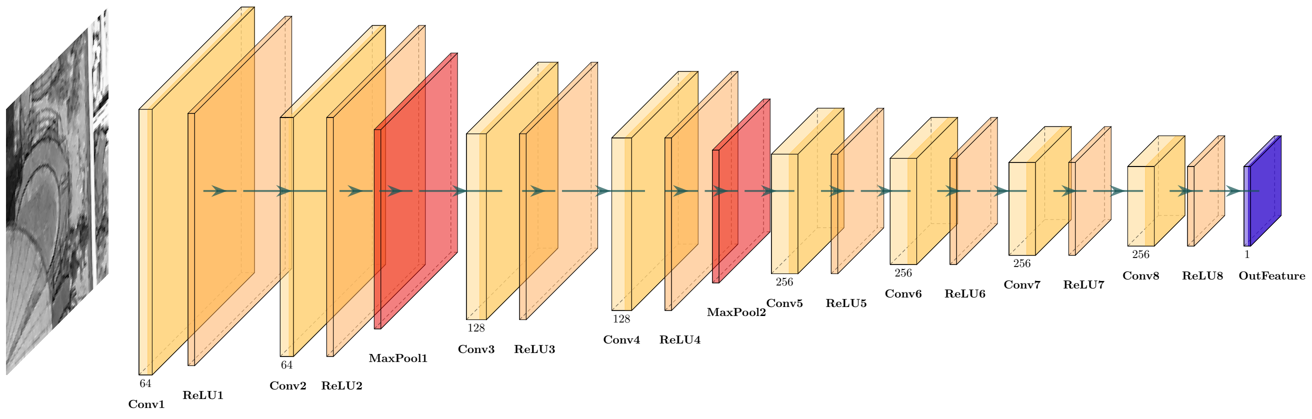

Figure 3: Architecture of feature extractor network.

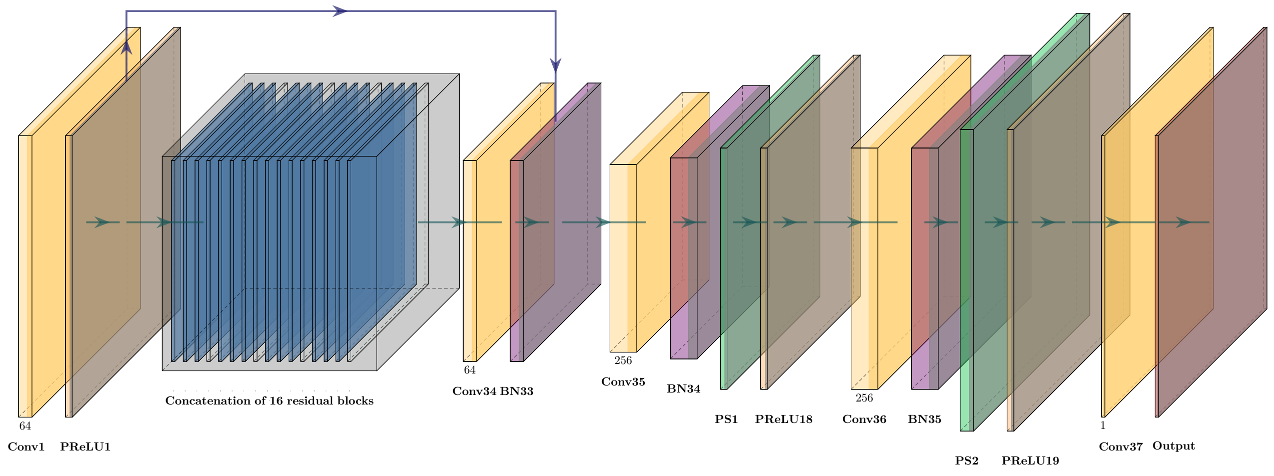

Figure 4: Architecture of generative network.

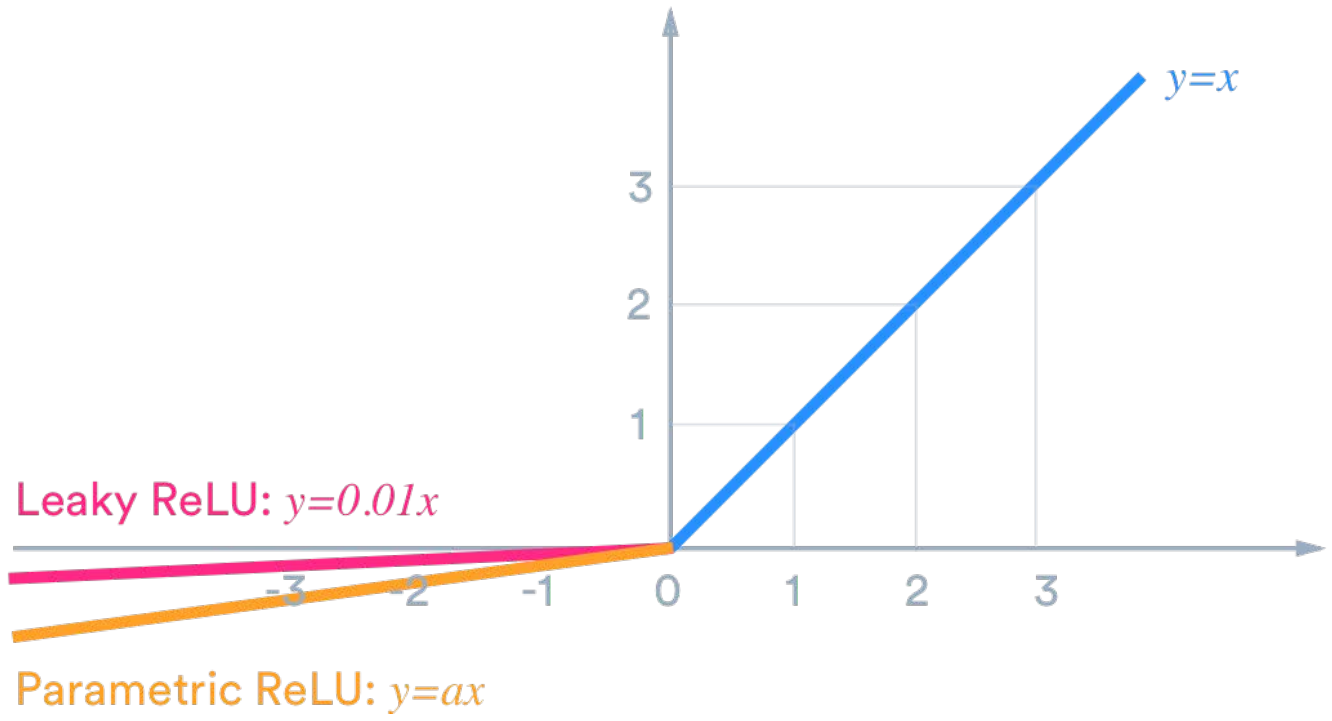

Figure 5: Representation of LReLU and PReLU.

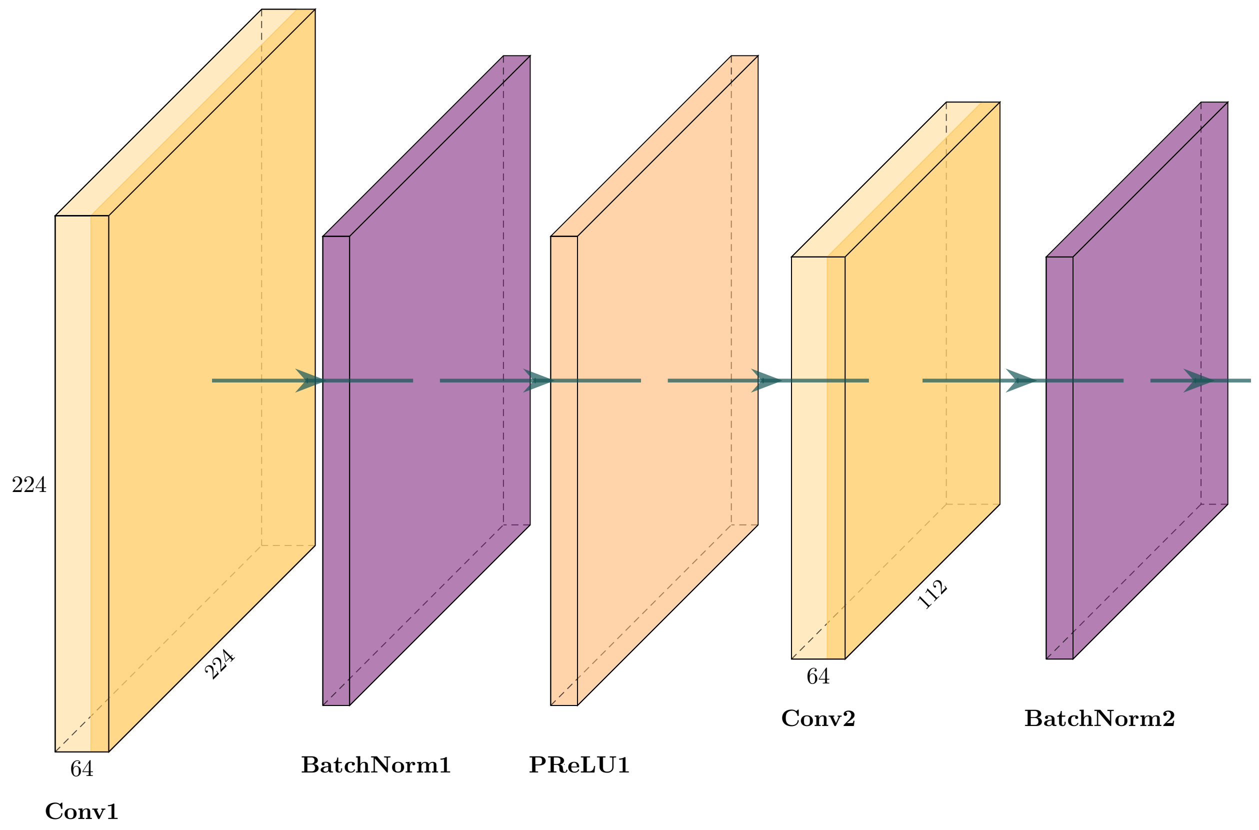

Figure 6: Architecture of residual block.

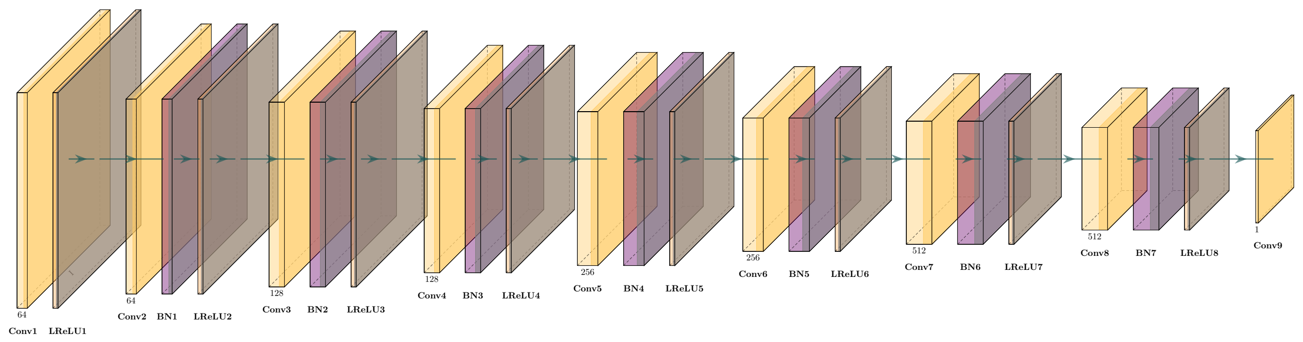

Figure 7: Architecture of discriminator network.

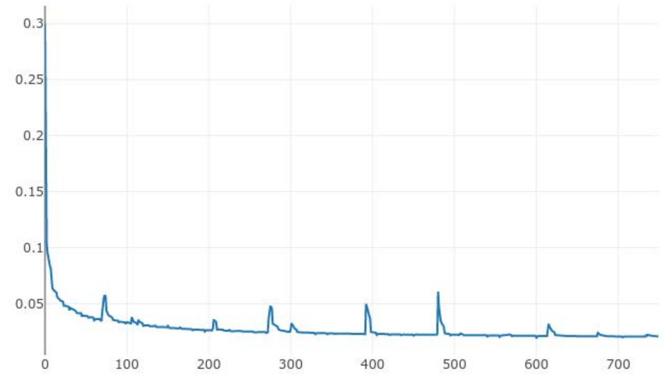
(a)

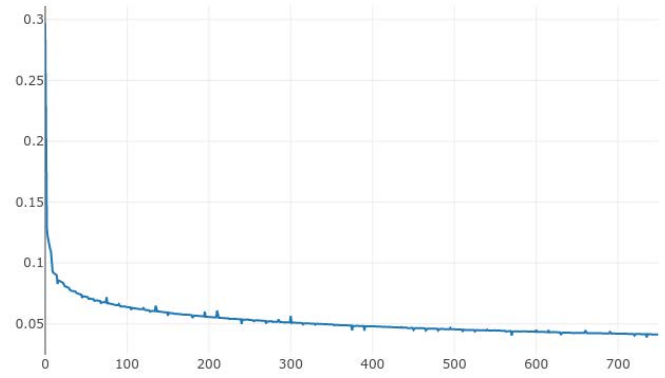
(b)

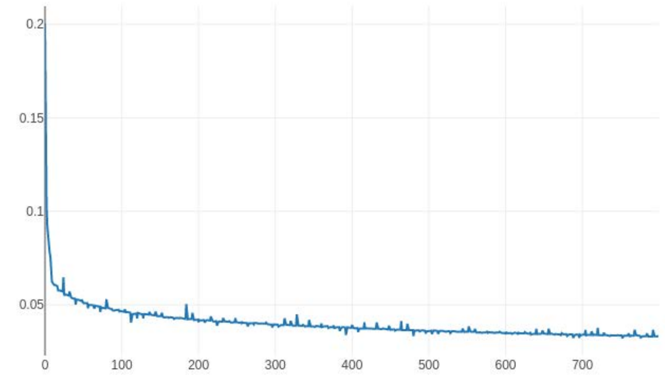
(c)

Figure 8: Batch con loss. (a) Group 1, (b) Group 2, (c) Group 3.

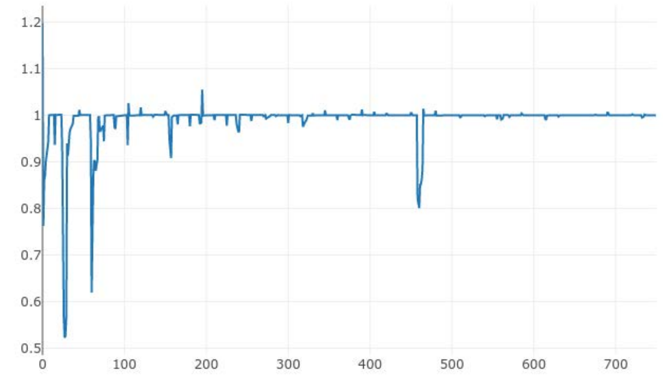
(a)

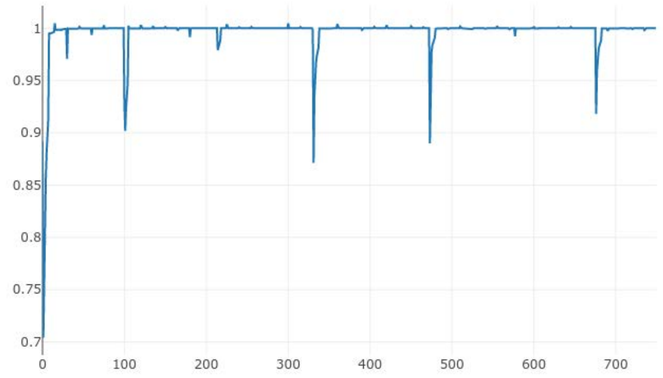
(b)

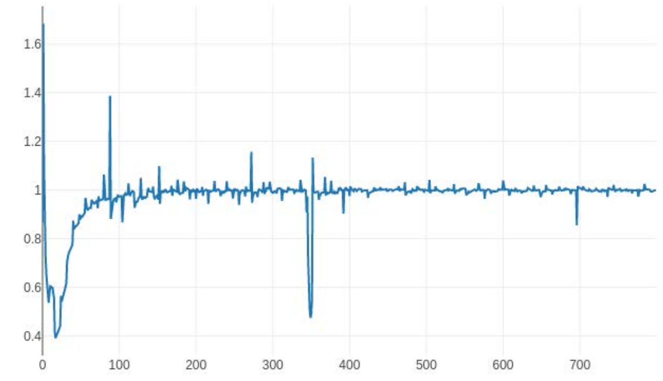
(c)

Figure 9: Batch gen los. (a) Group 1, (b) Group 2, (c) Group 3.

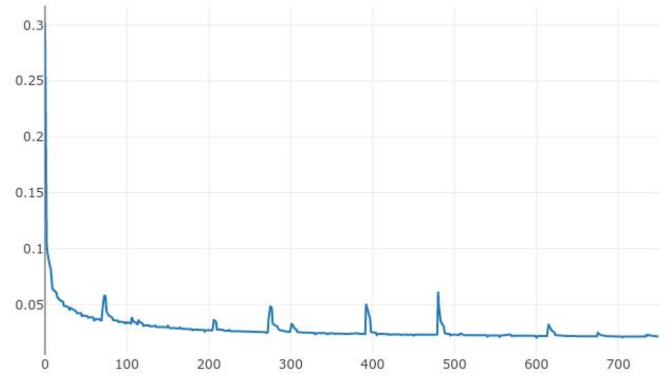

(a)

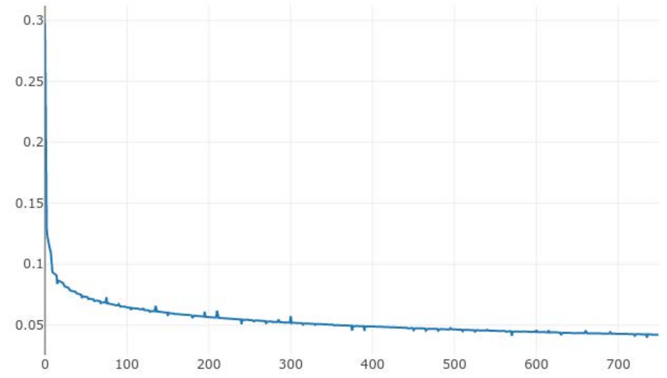

(b)

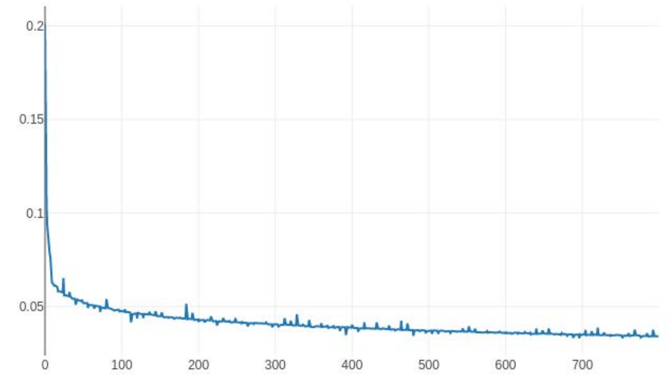

(c)

Figure 10: Batch G loss. (a) Group 1, (b) Group 2, (c) Group 3.

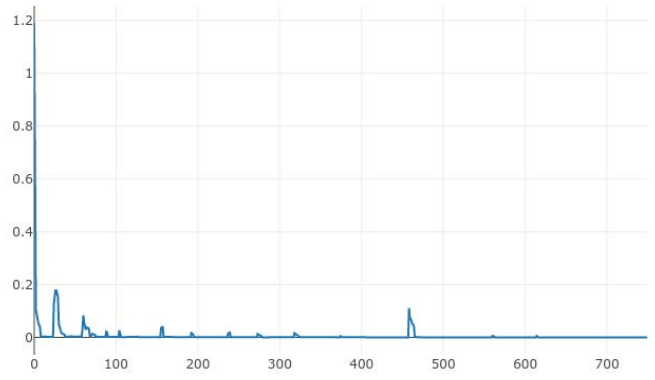

(a)

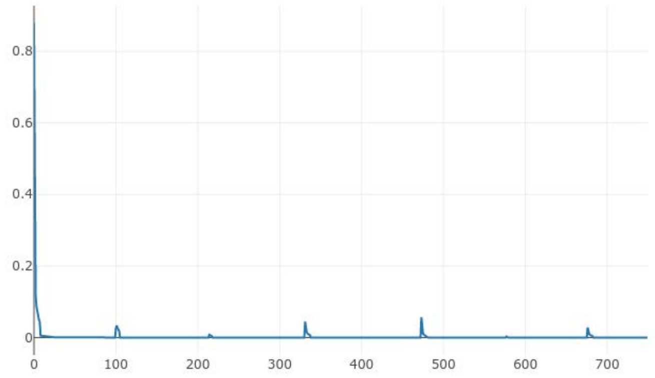

(b)

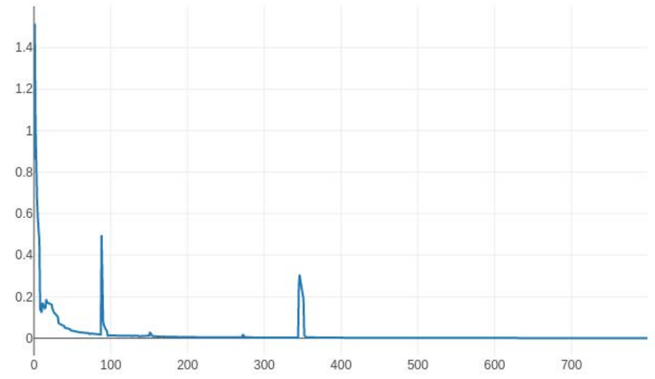

(c)

Figure 11: Batch real loss. (a) Group 1, (b) Group 2, (c) Group 3.

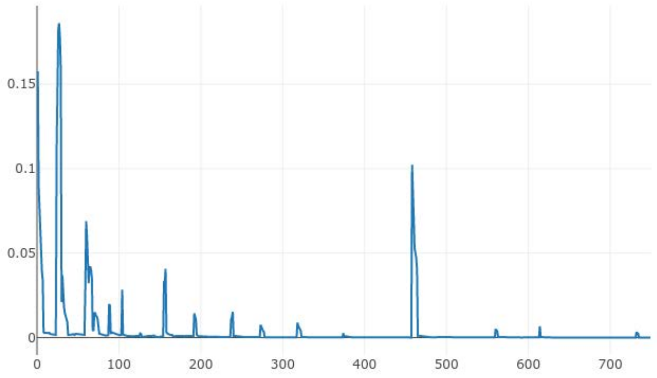

(a)

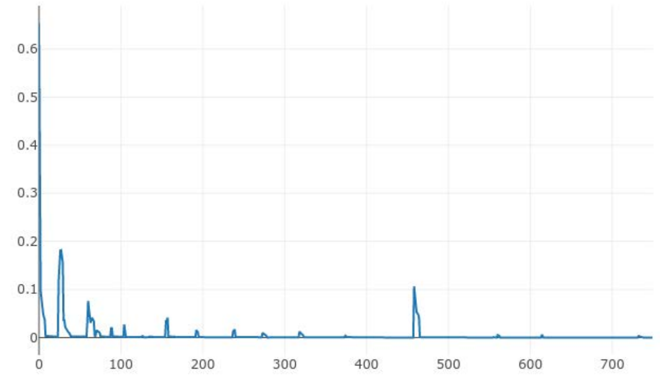

(a)

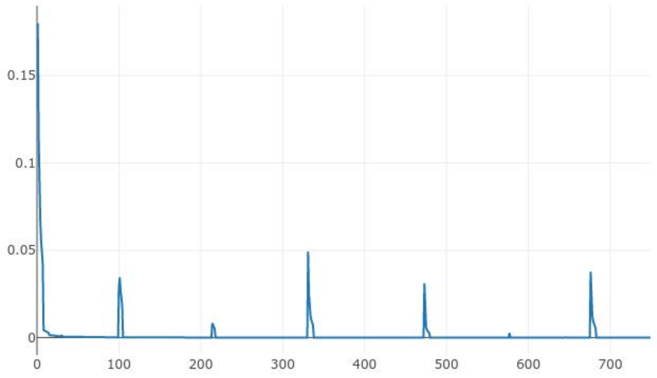

(b)

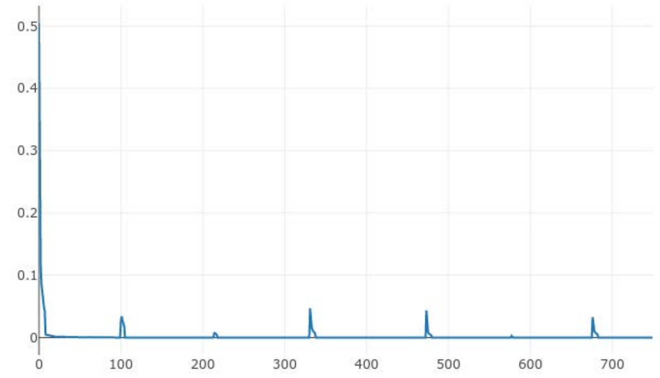

(b)

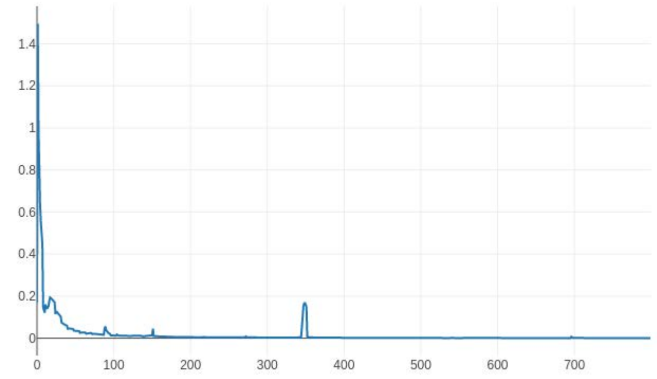

(c)

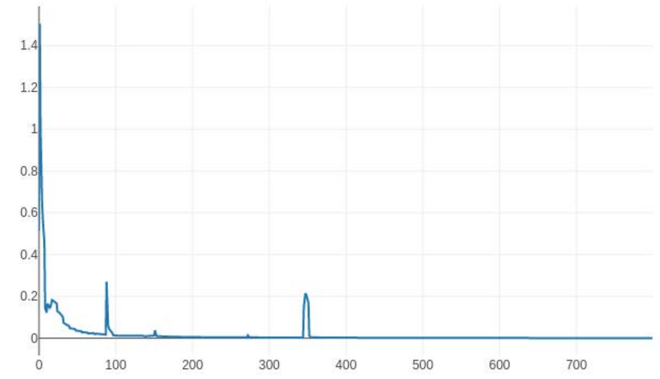

(c)

Figure 12: Batch fake loss. (a) Group 1, (b) Group 2, (c) Group 3.

Figure 13: Batch D loss. (a) Group 1, (b) Group 2, (c) Group 3.

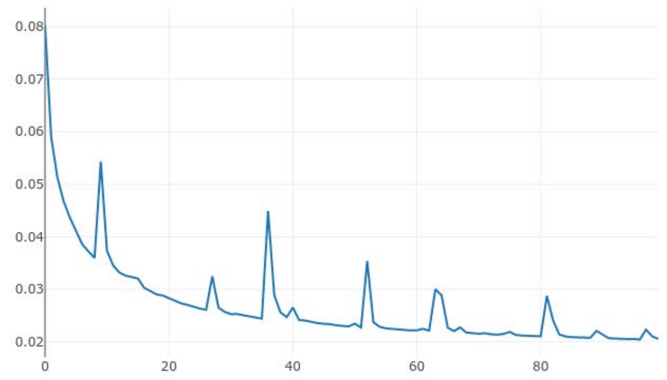

(a)

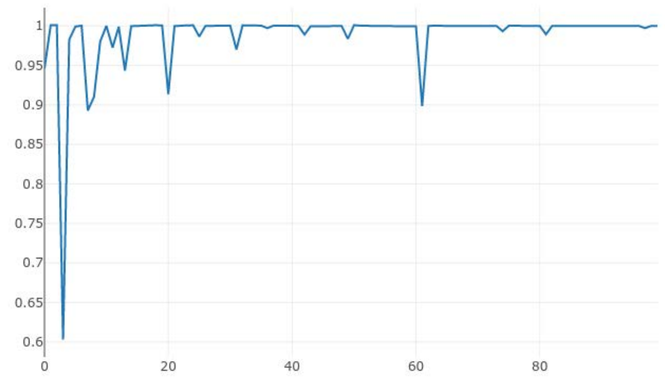

(a)

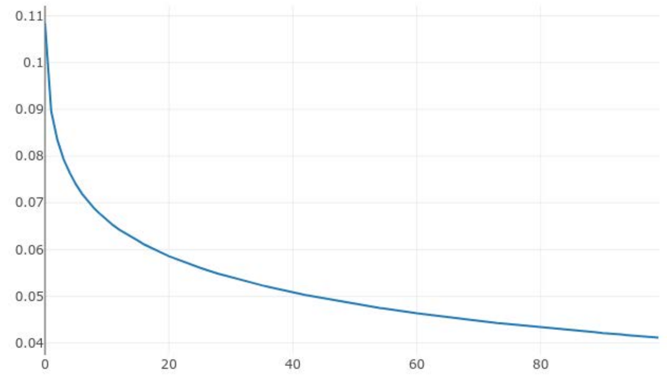

(b)

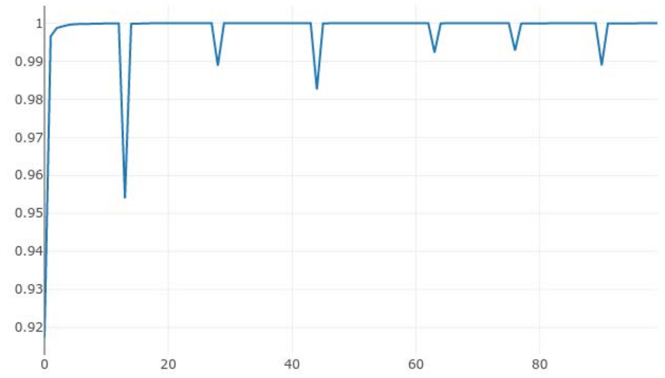

(b)

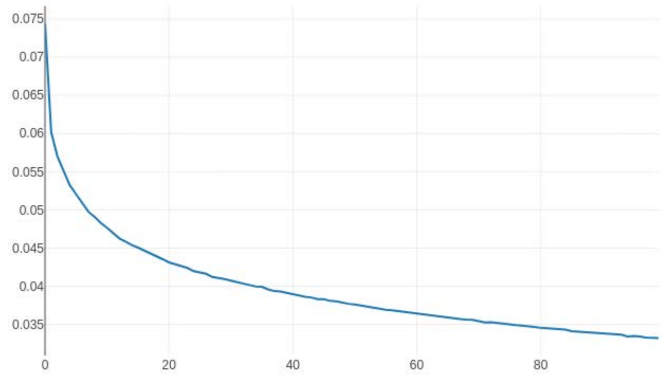

(c)

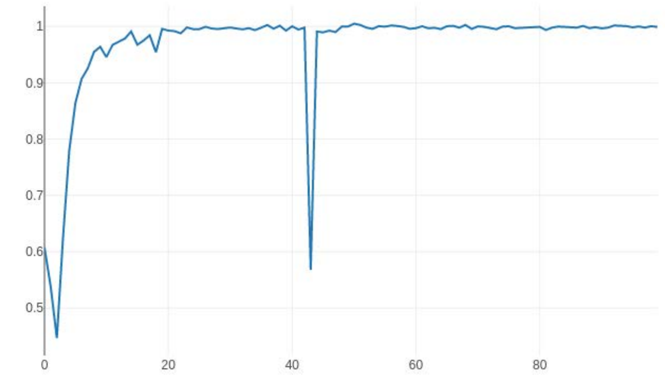

(c)

Figure 14: Epoch con loss. (a) Group 1, (b) Group 2, (c) Group 3.

Figure 15: Epoch gen loss. (a) Group 1, (b) Group 2, (c) Group 3.

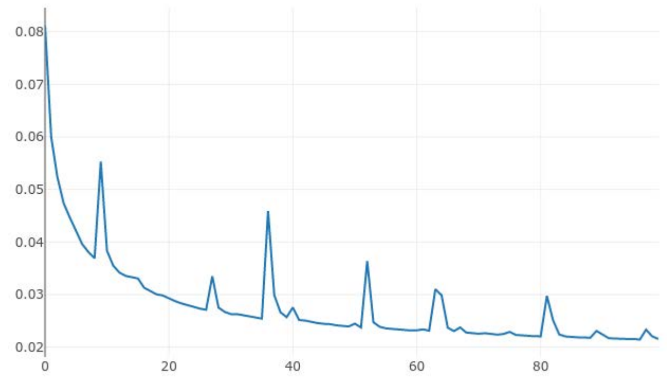

(a)

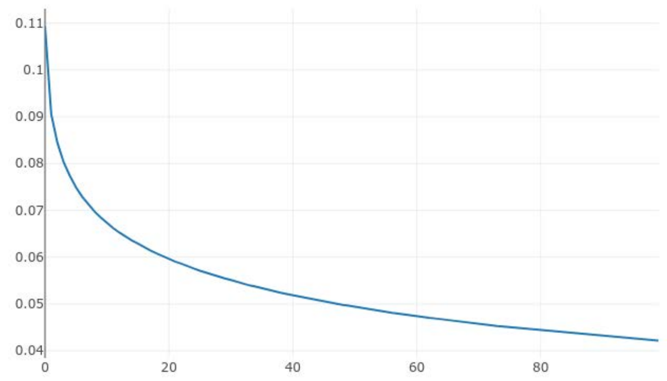

(b)

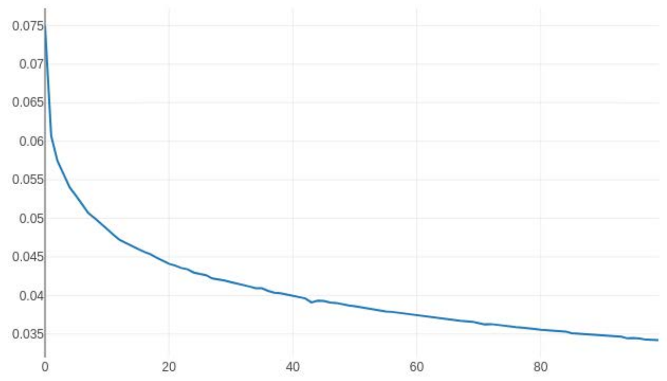

(c)

Figure 16: Epoch G loss. (a) Group 1, (b) Group 2, (c) Group 3.

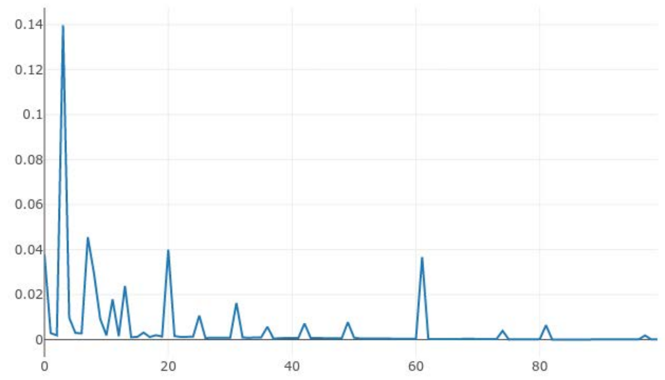

(a)

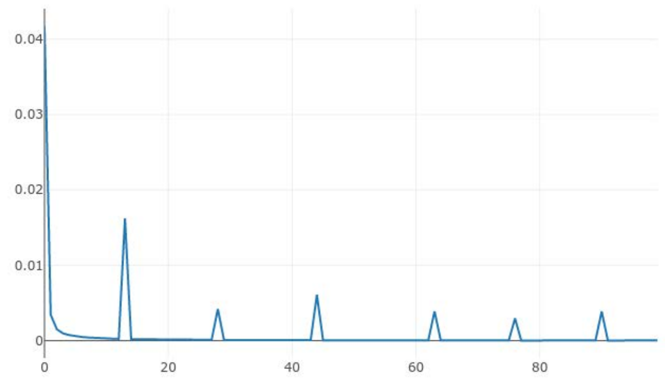

(b)

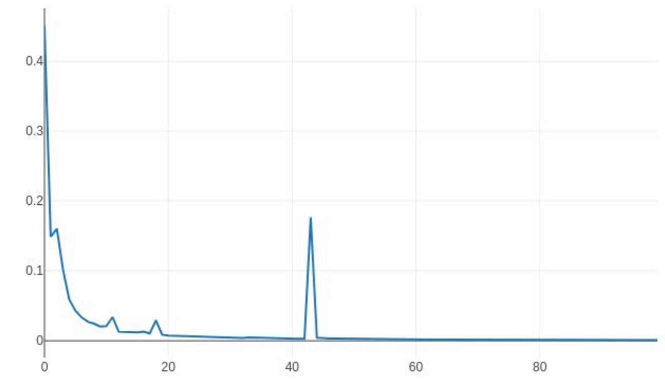

(c)

Figure 17: Epoch real loss. (a) Group 1, (b) Group 2, (c) Group 3.

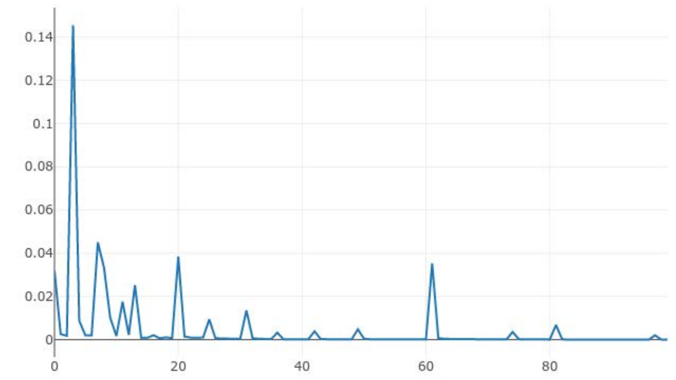
(a)

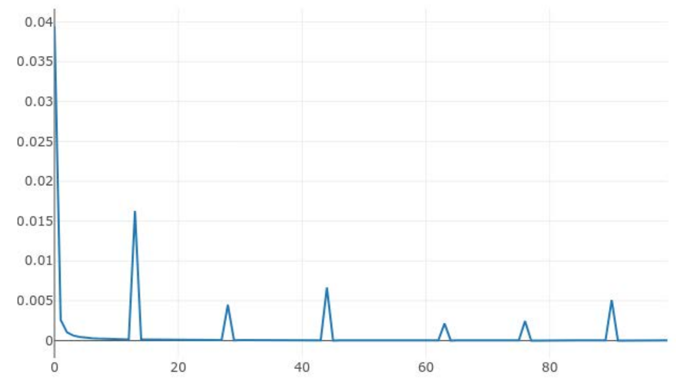
(b)

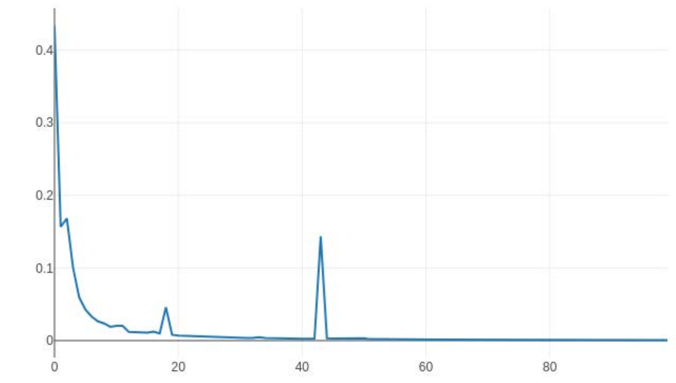
(c)

Figure 18: Epoch fake loss. (a) Group 1, (b) Group 2, (c) Group 3.

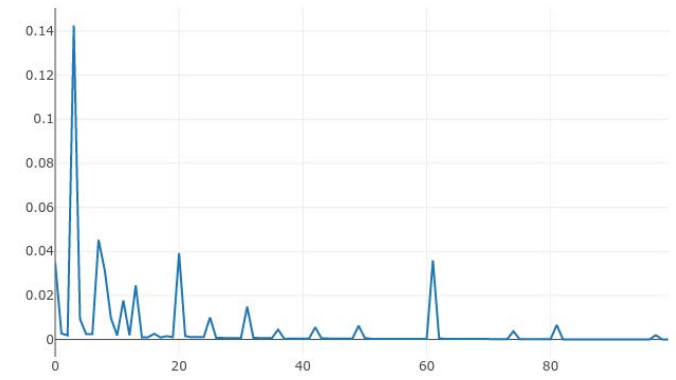
(a)

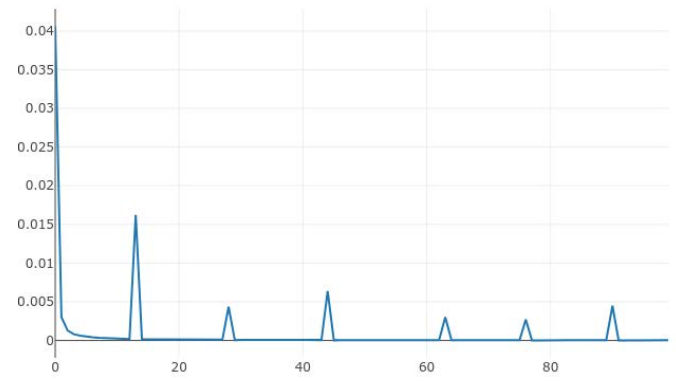
(b)

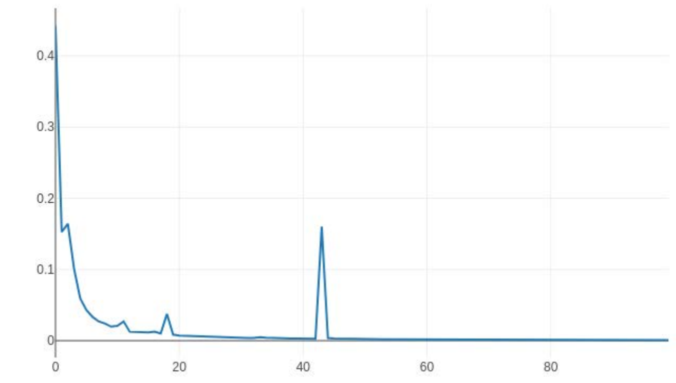
(c)

Figure 19: Epoch D loss. (a) Group 1, (b) Group 2, (c) Group 3.

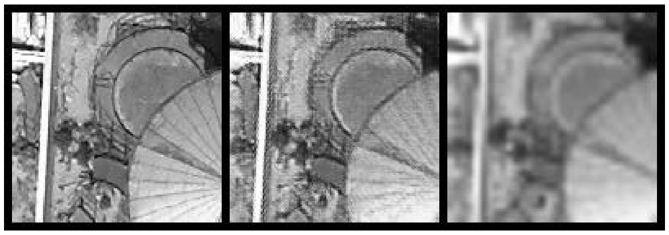

(a)

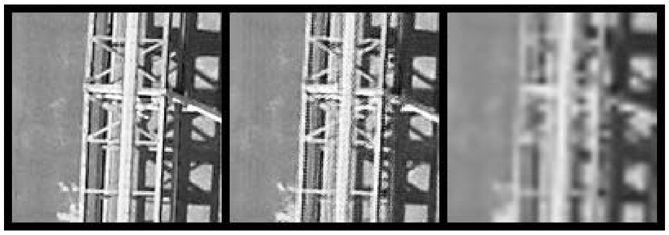

(b)

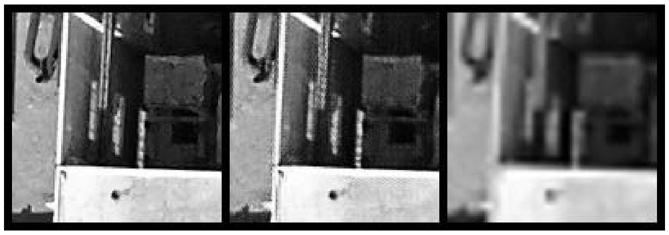

(c)

Figure 20: Reconstructed results by Group 1 (Ground truth, pbiSRGAN and Bicubic reconstruction are listed from left to right). (a) Oil tank, (b) Metal, (c) Roof.

No.	Parameters	Value
1	Operating system	Linux Ubuntu18.04
2	GPU model	Telsa K80
3	GPU memory	10GB
4	GPU number	3
5	CUDA version	10.2
6	CPU model	Intel Xeon(R)
7	CPU memory	47GB
8	CPU clock speed	2.5GHz
9	CPU core number	12
10	CPU number	4

Table 2: Hardware information for simulation.

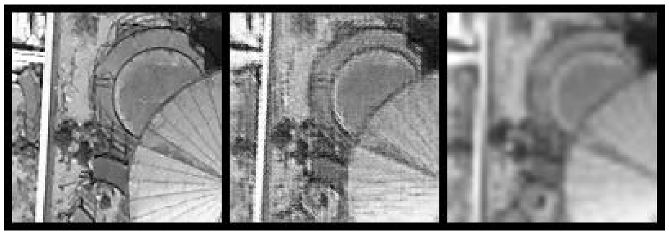

(a)

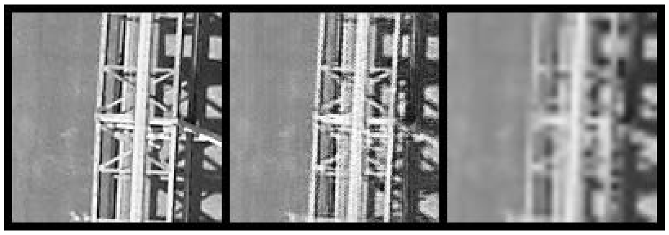

(b)

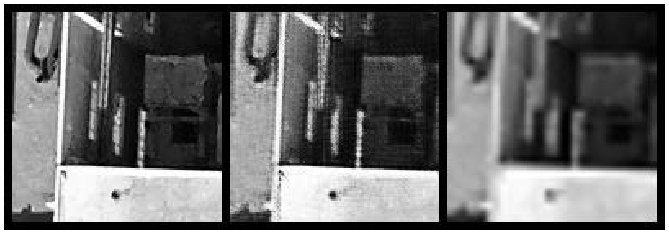

(c)

Figure 21: Reconstructed results by Group 2 (Ground truth, pbiSRGAN and Bicubic reconstruction are listed from left to right). (a) Oil tank, (b) Metal, (c) Roof.

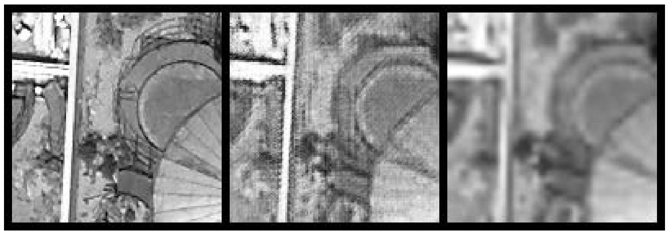

(a)

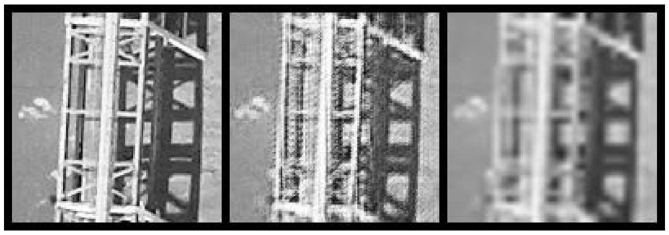

(b)

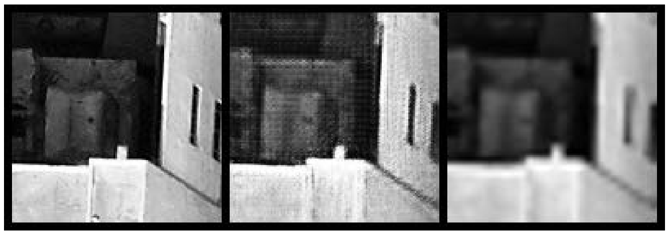

(c)

Figure 22: Reconstructed results by Group 3 (Ground truth, pbiSRGAN and Bicubic reconstruction are listed from left to right). (a) Oil tank, (b) Metal, (c) Roof.

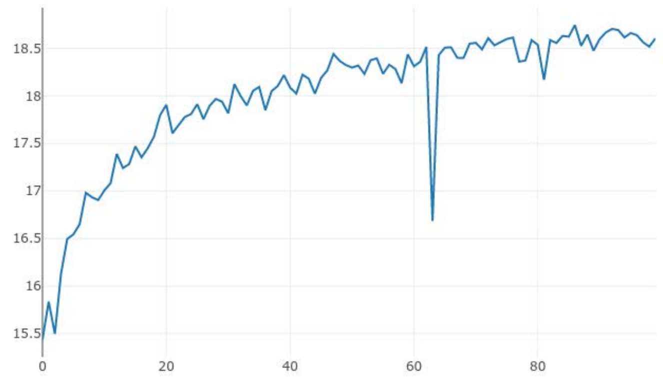

(a)

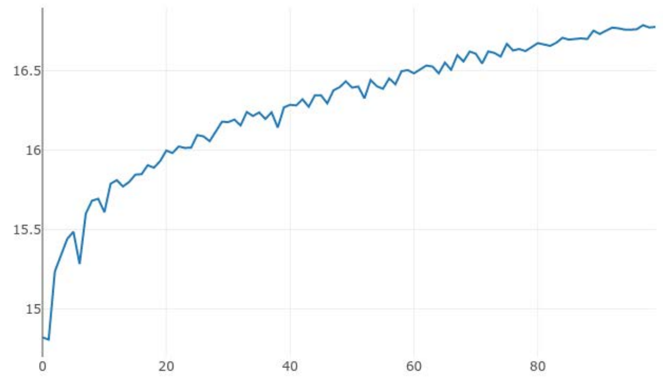

(b)

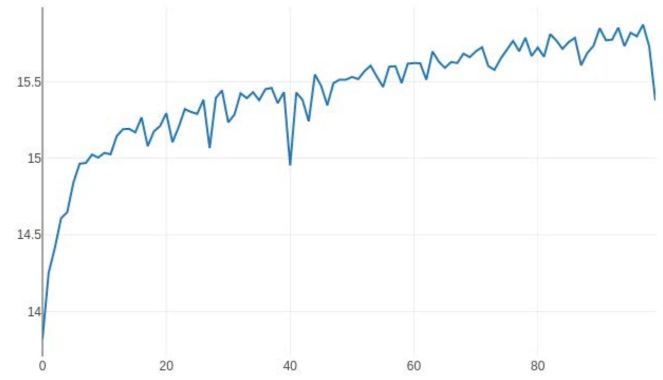

(c)

Figure 23: Mean PSNR of reconstructed results from validation set. (a) Group 1, (b) Group 2, (c) Group 3.

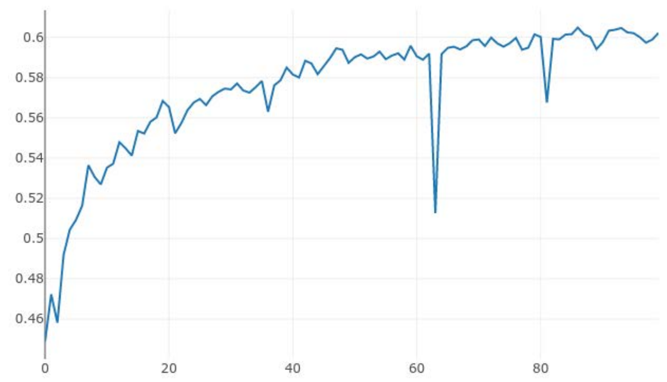

(a)

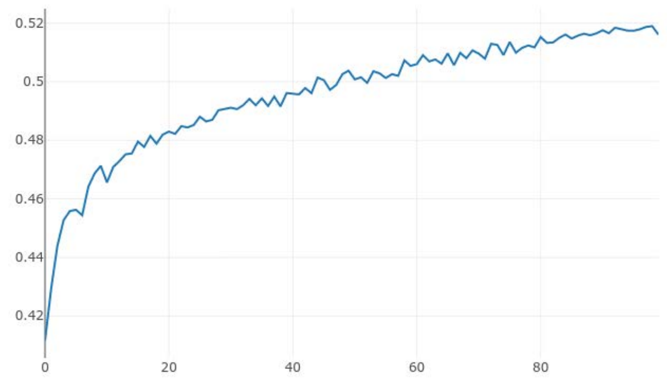

(b)

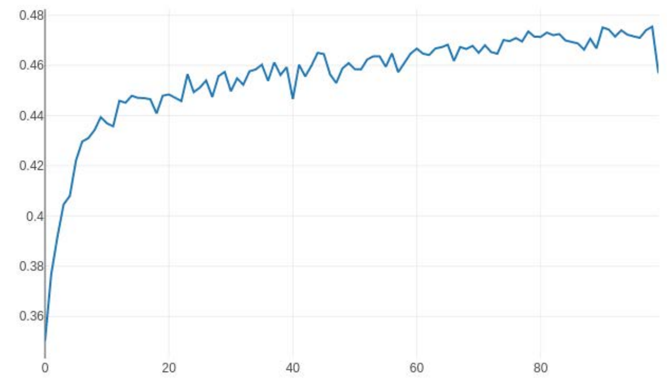

(c)

Figure 24: Mean SSIM of reconstructed results from validation set. (a) Group 1, (b) Group 2, (c) Group 3.

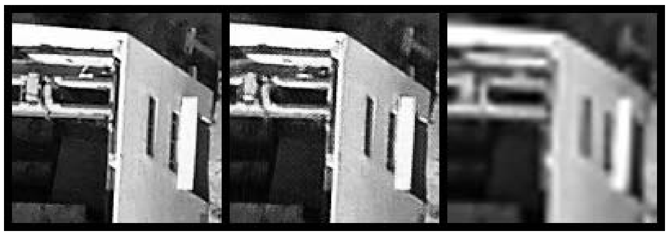

(a)

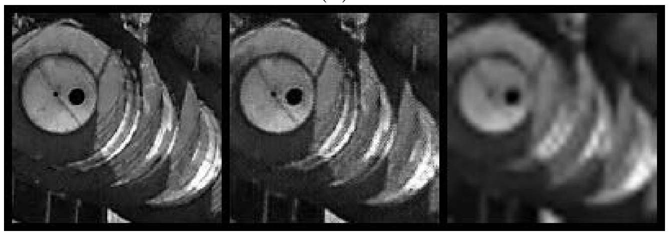

(b)

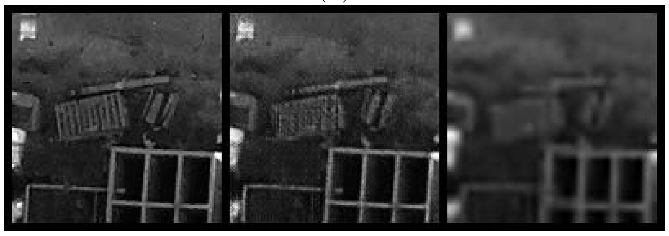

(c)

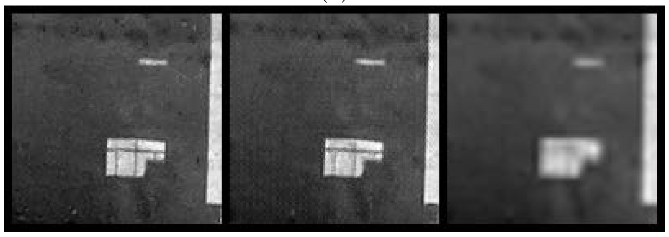

(d)

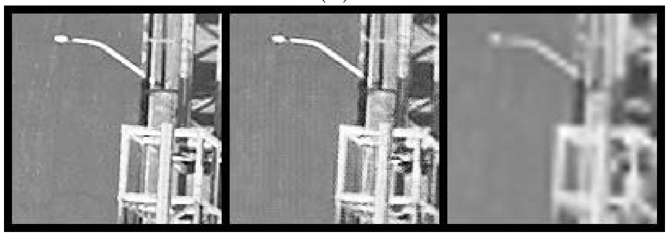

(e)

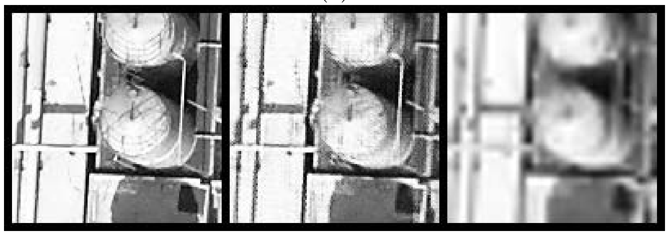

(f)

Figure 25: Part of Reconstructed results on testing set (Ground truth, pbiSRGAN and Bicubic reconstruction are listed from left to right). (a) Reconstruction 1, (b) Reconstruction 2 ,(c) Reconstruction 3, (d) Reconstruction 4, (e) Reconstruction 5, (f) Reconstruction 6.

Hyperparameters	Group 1	Group 2	Group 3
Traing epochs	100	100	100
Training batch size	128	128	128
Validation batch size	1	1	1
G learning rate	0.0002	0.0002	0.0002
D learning rate	0.0002	0.0002	0.0002
Epoch of learning rate decay	-	50	-
Percentage of learning rate decay	-	90%	-
Scaling factor	4	4	4
Training ratio of G and D	1:1	1:1	5:1
GPU number	3	3	3
Height of HR images	128	128	128
Width of HR images	128	128	128
Number of training images	96000	96000	96000
Number of validating images	3000	3000	3000
Number of testing images	1000	1000	1000

Table 3: Experimental scheme of pbiSRGAN

No.	Evaluation indicator	Group 1	Group 2	Group 3
1	PSNR	19.6652	17.9452	16.4628
2	SSIM	0.6045	0.5178	0.4575

Table 5: Mean PSNR and SSIM of reconstructed results from testing set.

No.	loss
1	batch con loss
2	batch gen loss
3	batch G loss
4	batch real loss
5	batch fake loss
6	batch D loss
7	epoch con loss
8	epoch gen loss
9	epoch G loss
10	epoch real loss
11	epoch fake loss
12	epoch D loss

Table 4: Two kinds of loss metrics: batch loss and epoch loss.